
p -Poisson surface reconstruction in irrotational flow from point clouds

Anonymous Author(s)

Affiliation

Address

email

Abstract

1 The aim of this paper is the reconstruction of a smooth surface from an unorga-
2 nized point cloud sampled by a closed surface, with the preservation of geometric
3 shapes, without any further information other than the point cloud. Implicit neural
4 representations (INRs) have recently emerged as a promising approach to surface
5 reconstruction. However, the reconstruction quality of existing methods relies on
6 ground truth implicit function values or surface normal vectors. In this paper, we
7 show that proper supervision of partial differential equations and fundamental prop-
8 erties of differential vector fields are sufficient to robustly reconstruct high-quality
9 surfaces. We cast the p -Poisson equation to learn a signed distance function (SDF)
10 and the reconstructed surface is implicitly represented by the zero-level set of the
11 SDF. For efficient training, we develop a variable splitting structure by introducing
12 a gradient of the SDF as an auxiliary variable and impose the p -Poisson equation
13 directly on the auxiliary variable as a hard constraint. Based on the irrotational
14 property of the gradient field, we impose a curl-free constraint on the auxiliary
15 variable, which leads to a more faithful reconstruction. Experiments on standard
16 benchmark datasets show that the proposed INR provides a superior and robust
17 reconstruction.

18 1 Introduction

19 Surface reconstruction from an un-
20 organized point cloud has been exten-
21 sively studied for more than two
22 decades [10, 28, 38, 9, 60] due to
23 its many downstream applications
24 in computer vision and computer
25 graphics[8, 16, 60, 56]. Classical
26 point cloud or mesh-based representa-
27 tions are efficient but they do not guar-
28 antee a watertight surface and are usu-
29 ally limited to fixed geometries. Im-
30 plicit function-based representations
31 of the surface [27, 62, 41, 14] as a
32 level set $\mathcal{S} = \{\mathbf{x} \in \mathbb{R}^3 \mid u(\mathbf{x}) = c\}$
33 of a continuous implicit function $u : \mathbb{R}^3 \rightarrow \mathbb{R}$, such as signed distance
34 functions (SDFs) or occupancy func-
35 tions, have received considerable attention for providing watertight results and great flexibility in
36 representing different topologies. In recent years, with the rise of deep learning, a stream of work
37

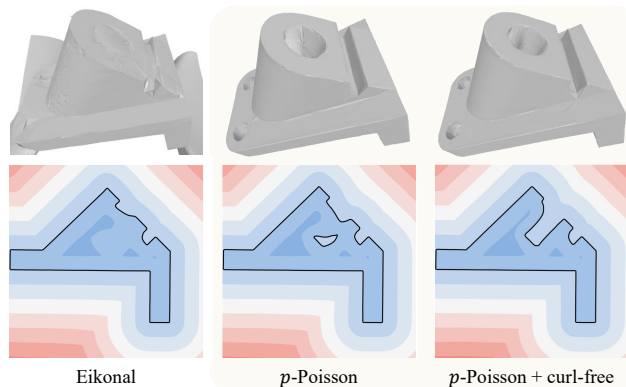


Figure 1: Comparison of a naive approach (9), the p -Poisson equation (8), and the proposed p -Poisson equation with the curl-free condition (11).

38 called *implicit neural representations* (INRs) [2, 42, 16, 59, 19, 53, 51, 48] has revisited them by
 39 parameterizing the implicit function u with neural networks. INRs have shown promising results by
 40 offering efficient training and expressive surface reconstruction.

41 Early INRs [42, 40, 16] treat the points-to-surface problem as a supervised regression problem with
 42 ground-truth distance values, which are difficult to use in many situations. To overcome this limitation,
 43 some research efforts have used partial differential equations (PDEs), typically the eikonal equation,
 44 as a means to relax the 3D supervision [23, 35, 46]. While these efforts have been successful in
 45 reconstructing various geometries, they rely heavily on the oriented normal vector at each point.
 46 They often fail to capture fine details or reconstruct plausible surfaces without normal vectors. A raw
 47 point cloud usually lacks normal vectors or numerically estimated normal vectors [1, 18] contain
 48 approximation errors. Moreover, the prior works are vulnerable to noisy observations and outliers.

49 The goal of this work is to propose an implicit representation of surfaces that not only provides
 50 smooth reconstruction but also recovers high-frequency features only from a raw point cloud. To this
 51 end, we provide a novel approach that expresses an approximated SDF as a solution to the p -Poisson
 52 equation. In contrast to previous studies that only describe the SDF as a network, we define the
 53 gradient of the SDF as an auxiliary variable, motivated by variable splitting methods [45, 58, 22, 12]
 54 in the optimization literature. We then parameterize the auxiliary output to automatically satisfy the
 55 p -Poisson equation by reformulating the equation in a divergence-free form. The divergence-free
 56 splitting representation contributes to efficient training by avoiding deeply nested gradient chains
 57 and allows the use of sufficiently large p , which permits an accurate approximation of the SDF. In
 58 addition, we impose a curl-free constraint [25] because the auxiliary variable should be learned as
 59 a conservative vector field. The curl-free constraint serves to achieve a faithful reconstruction. We
 60 carefully evaluate the proposed model on widely used benchmarks and robustness to noise. The
 61 results demonstrate the superiority of our model without a priori knowledge of the surface normal at
 62 the data points.

63 2 Background and related works

64 **Implicit neural representations** In recent years, implicit neural representations (INRs) [39, 16, 3,
 65 53, 52], which define a surface as zero level-sets of neural networks, have been extensively studied.
 66 Early work requires the ground-truth signed implicit function [42, 16, 39], which is difficult to obtain
 67 in real-world scenarios. Considerable research [3, 4] is devoted to removing 3D supervision and
 68 relaxing it with a ground truth normal vector at each point. In particular, several efforts use PDEs
 69 to remove supervision and learn implicit functions only from raw point clouds. Recently, IGR [23]
 70 revisits a conventional numerical approach [14] that accesses the SDF by incorporating the eikonal
 71 equation into a variational problem by using modern computational tools of deep learning. Without
 72 the normal vector, however, IGR misses fine details. To alleviate this problem, FFN [54] and SIREN
 73 [53] put the high frequencies directly into the network. Other approaches exploit additional loss terms
 74 to regulate the divergence [6] or the Hessian [61]. The vanishing viscosity method, which perturbs
 75 the eikonal equation with a small diffusion term, is also considered [35, 47] to mitigate the drawback
 76 that the eikonal loss has unreliable minima. The classical Poisson reconstruction [30], which recovers
 77 the implicit function by integration over the normal vector field, has also been revisited to accelerate
 78 the model inference time [46], but supervision of the normal vector field is required. Neural-Pull [37]
 79 constructs a new loss function by borrowing the geometrical property that the SDF and its gradient
 80 define the shortest path to the surface.

81 **p -Poisson equation** The SDF is described by a solution of various PDEs, such as the eikonal
 82 equation used in the existing work [23, 35, 47]. We use the p -Poisson equation to approximate the
 83 SDF, which is a nonlinear generalization of the Poisson equation ($p = 2$):

$$\begin{cases} -\Delta_p u = -\nabla \cdot (\|\nabla u\|^{p-2} \nabla u) = 1 \text{ in } \Omega \\ u = 0 \text{ on } \Gamma, \end{cases} \quad (1)$$

84 where $p \geq 2$, the computation domain $\Omega \subset \mathbb{R}^3$ is bounded, and Γ is embedded in Ω . In contrast to
 85 the eikonal equation, it is possible to describe a solution of (1) as a variational problem and compute
 86 an accurate approximation [5, 20]:

$$\min_u \int_{\Omega} \frac{\|\nabla u\|^p}{p} dx - \int_{\Omega} u dx. \quad (2)$$

87 As $p \rightarrow \infty$, it has been shown [11, 29] that the solution u of (1) converges to the SDF whose zero
 88 level set is Γ . As a result, increasing p gives a better approximation of the SDF, which is definitely
 89 helpful for surface reconstruction. However, it is still difficult to use a fairly large p in numerical
 90 computations and in this paper we will explain one of the possible solutions to the mentioned problem.

91 3 Method

92 In this section, we propose a p -Poisson equation based **Implicit Neural** representation with **Curl-free**
 93 **constraint (PINC)**. From an unorganized point cloud $\mathcal{X} = \{\mathbf{x}_i : i = 1, 2, \dots, N\}$ sampled by a
 94 closed surface Γ , a SDF $u : \mathbb{R}^3 \rightarrow \mathbb{R}$ whose zero level set is the surface $\Gamma = \{\mathbf{x} \in \mathbb{R}^3 \mid u(\mathbf{x}) = 0\}$
 95 is reconstructed by the proposed INR. There are two key elements in the proposed method: First,
 96 using a variable-splitting representation [43] of the network, an auxiliary output is used to learn
 97 the gradient of the SDF that satisfies the p -Poisson equation (1). Second, a curl-free constraint is
 98 enforced on an auxiliary variable to ensure that the differentiable vector identity is satisfied.

99 3.1 p -Poisson equation

100 A loss function in the physics-informed framework [49] of the existing INRs for the p -Poisson
 101 equation (1) can be directly written:

$$\min_u \int_{\Gamma} |u| d\mathbf{x} + \lambda_0 \int_{\Omega} \left| \nabla \cdot \left(\|\nabla u\|^{p-2} \nabla u \right) + 1 \right| d\mathbf{x}, \quad (3)$$

102 where $\lambda_0 > 0$ is a constant. To reduce the learning complexity of the second integrand, we propose
 103 an augmented network structure that separately parameterizes the gradient of the SDF as an auxiliary
 104 variable that satisfies the p -Poisson equation (1).

105 **Variable-splitting strategy** Unlike existing studies [23, 35, 6] that use neural networks with only
 106 one output u for the SDF, we introduce a separate auxiliary network output G for the gradient of
 107 the SDF. In the optimization literature, it is called the variable splitting method [45, 58, 22, 12] and
 108 it has the advantage of decomposing a complex minimization into a sequence of relatively simple
 109 sub-problems. With the auxiliary variable $G = \nabla u$ and the penalty method [13], the variational
 110 problem (3) is converted into an unconstrained problem:

$$\min_{u,G} \int_{\Gamma} |u| d\mathbf{x} + \lambda_0 \int_{\Omega} \left| \nabla \cdot \left(\|G\|^{p-2} G \right) + 1 \right| d\mathbf{x} + \lambda_1 \int_{\Omega} \|\nabla u - G\|^2 d\mathbf{x}, \quad (4)$$

111 where $\lambda_1 > 0$ is a penalty parameter representing the relative importance of the loss terms.

112 **p -Poisson as a hard constraint** Looking more closely at the minimization (4), if G is already a
 113 gradient to satisfy (1), then the second term in (4) is no longer needed and it brings the simplicity of
 114 one less parameter. Now, for a function $F : \Omega \rightarrow \mathbb{R}^3$ such that $\nabla \cdot F = 1$, for example $F = \frac{1}{3}\mathbf{x}$, the
 115 p -Poisson equation (1) is reformulated by the divergence-free form:

$$\nabla \cdot \left(\|\nabla u\|^{p-2} \nabla u + F \right) = 0. \quad (5)$$

116 Then, there exists a vector potential $\Psi : \mathbb{R}^3 \rightarrow \mathbb{R}^3$ satisfying

$$\|G\|^{p-2} G + F = \nabla \times \Psi, \quad (6)$$

117 where $G = \nabla u$. Note that a similar idea is used in the neural conservation law [50] to construct a
 118 divergence-free vector field built on the Helmholtz decomposition [32, 55]. From the condition (6),
 119 we have $\|G\|^{p-1} = \|\nabla \times \Psi - F\|$ and G is parallel to $\nabla \times \Psi - F$, then the auxiliary output G is
 120 explicitly written:

$$G = \frac{\nabla \times \Psi - F}{\|\nabla \times \Psi - F\|^{\frac{p-2}{p-1}}}. \quad (7)$$

121 This confirms that the minimization problem (4) does not require finding G directly, but rather that it
 122 can be obtained from the vector potential Ψ . Therefore, the second loss term in (4) can be eliminated

123 by approximating the potential function Ψ by a neural network and defining the auxiliary output G as
 124 a hard constraint (7). To sum up, we use a loss function of the form

$$\mathcal{L}_{p\text{-Poisson}} = \int_{\Gamma} |u| d\mathbf{x} + \lambda_1 \int_{\Omega} \|\nabla u - G\|^2 d\mathbf{x}, \quad (8)$$

125 where G is obtained by (7), the first term is responsible for imposing the boundary condition of (1),
 126 and the second term enforces the constraint $G = \nabla u$ between primary and auxiliary outputs. It is
 127 worth mentioning that G in (7) is designed to exactly satisfy the p -Poisson equation (1).

128 An advantage of the proposed loss function (8) and the hard constraint (7) is that (1) can be solved
 129 for sufficiently large p , which is critical to make a better approximation of the SDF. It is not
 130 straightforward in (3) or (4) because the numeric value of $(p-2)$ -power with a large p easily exceeds
 131 the limit of floating precision. On the other hand, in (7) we use $(p-2)/(p-1)$ -power, which allows
 132 stable computation even when p becomes arbitrarily large. The surface reconstruction with varying
 133 p in Figure 7 shows that using a large enough p is crucial to get a good reconstruction. As the p
 134 increases, the reconstruction gets closer and closer to the point cloud. Furthermore, it is worth noting
 135 that the proposed representation expresses the second-order PDE (1) with first-order derivatives only.
 136 By reducing the order of the derivatives, the computational graph is simplified than (3) or (4).

137 Note that one can think of an approach to directly solve the eikonal equation $\|\nabla u\| = 1$ with an
 138 auxiliary variable $H = \nabla u$ as an output of the neural network:

$$\min_{u, \|H\|=1} \int_{\Gamma} |u| d\mathbf{x} + \eta \int_{\Omega} \|\nabla u - H\|^2 d\mathbf{x}, \quad (9)$$

139 where $\eta > 0$. The above loss function may produce a non-unique weak solution of the eikonal
 140 equation, which causes numerical instability and undesirable estimation of the surface reconstruction;
 141 see Figure 1. To alleviate such an issue, the vanishing viscosity method is used in [35, 47] to
 142 approximate the SDF by u_{σ} as $\sigma \rightarrow 0$, a solution of $-\sigma \Delta u_{\sigma} + \text{sign}(u_{\sigma})(|\nabla u_{\sigma}| - 1) = 0$. However,
 143 the results are dependent on the hyper-parameter $\sigma > 0$ related to the resolution of the discretized
 144 computational domain and the order of the numerical scheme [17, 24].

145 3.2 Curl-free constraint

146 In the penalty method, we have to compute more strictly to ensure that $G = \nabla u$ by using progressively
 147 larger values of λ_1 in (8), but in practice we cannot make the value of λ_1 infinitely large. Now, we
 148 can think of yet another condition for enforcing the constraint $G = \nabla u$ from a differential vector
 149 identity:

$$\nabla \times G = 0 \iff G = \nabla u \quad (10)$$

150 for some scalar potential function u . While it may seem straightforward, adding a penalty term
 151 $\int_{\Omega} \|\nabla \times G\|^2 d\mathbf{x}$ at the top of (8) is fraught with problems. Since G is calculated by using a curl
 152 operation (7), the mentioned penalty term makes a long and complex computational graph. In
 153 addition, it has been reported that such loss functions, which include high-order derivatives computed
 154 by automatic differentiation, induce a loss landscape that is difficult to optimize [33, 57]. In order to
 155 relax the mentioned issue, we augment another auxiliary variable \tilde{G} , where $G = \tilde{G}$ and $\nabla \times \tilde{G} = 0$
 156 are constrained.

157 By incorporating the new auxiliary variable \tilde{G} and its curl-free constraint, we have the following loss
 158 function:

$$\mathcal{L}_{\text{PINC}} = \mathcal{L}_{p\text{-Poisson}} + \lambda_2 \int_{\Omega} \|G - \tilde{G}\|^2 d\mathbf{x} + \lambda_3 \int_{\Omega} \|\nabla \times \tilde{G}\|^2 d\mathbf{x}. \quad (11)$$

159 Note that the optimal \tilde{G} should have a unit norm according to the eikonal equation. To facilitate
 160 training, we relax this nonconvex equality condition into a convex constraint $\|\tilde{G}\| \leq 1$. To this end,
 161 we parameterize the second network auxiliary output $\tilde{\Psi}$ and define \tilde{G} by

$$\tilde{G} = \mathcal{P}(\tilde{\Psi}) := \frac{\tilde{\Psi}}{\max\{1, \|\tilde{\Psi}\|\}}, \quad (12)$$

162 where \mathcal{P} is the projection operator to the three-dimensional unit ball.

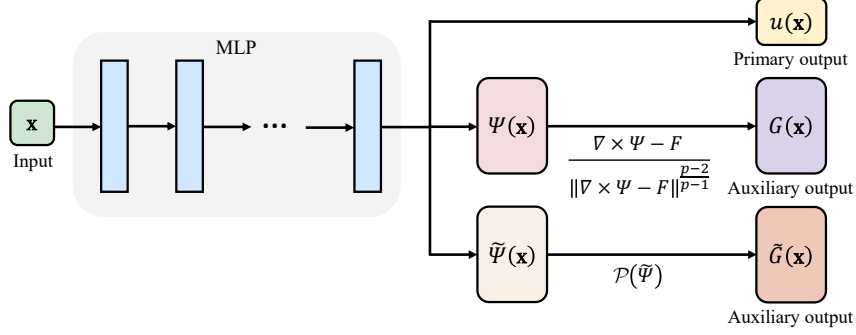


Figure 2: The visualization of the augmented network structure with two auxiliary variables.

163 Figure 2 illustrates the proposed network architecture. The primary and the auxiliary variables are
 164 trained in a single network, instead of being trained separately in individual networks. The number
 165 of network parameters remains almost the same since only the output dimension of the last layer is
 166 increased by six, while all hidden layers are shared.

167 3.3 Proposed loss function

168 In the case of a real point cloud to estimate a closed surface by range scanners, it is inevitable to have
 169 occluded parts of the surface where the surface has a concave part depending on possible angles of
 170 the measurement [34]. It ends up having relatively large holes in the measured point cloud. Since
 171 there are no points in the middle of the hole, it is necessary to have a certain criterion for how to fill
 172 in the hole. In order to focus to check the quality of $\mathcal{L}_{\text{PINC}}$ (11) in this paper, we choose a simple rule
 173 to minimize the area of zero level set of u :

$$\mathcal{L}_{\text{total}} = \mathcal{L}_{\text{PINC}} + \lambda_4 \int_{\Omega} \delta_{\epsilon}(u) \|\nabla u\| d\mathbf{x}, \quad (13)$$

174 where $\lambda_4 > 0$ and $\delta_{\epsilon}(x) = 1 - \tanh^2\left(\frac{x}{\epsilon}\right)$ is a smeared Dirac delta function with $\epsilon > 0$. The
 175 minimization of the area is used in [21, 47] and the advanced models [15, 26, 61] on missing parts of
 176 the point cloud provide better performance of the reconstruction.

177 4 Experimental results

178 In this section, we evaluate the performance of the proposed model to reconstruct 3D surfaces from
 179 point clouds. We study the following questions: **(i)** How does the proposed model perform compared
 180 to existing INRs? **(ii)** Is it stable from noise? **(iii)** What is the role of the parts that make up the model
 181 and the loss? Each is elaborated in order in the following sections.

182 **Implementation** As in previous studies [42, 23, 35], we use an 8-layer network with 512 neurons
 183 and a skip connection to the middle layer, but only the output dimension of the last layer is increased
 184 by six due to the auxiliary variables. For (13), we empirically set the loss coefficients to $\lambda_1 = 0.1$,
 185 $\lambda_2 = 0.0001$, $\lambda_3 = 0.0005$, and $\lambda_4 = 0.1$ and use $p = \infty$ in (7) for numerical simplicity. We
 186 implement all numerical experiments on a single NVIDIA RTX 3090 GPU. In all experiments, we
 187 use the Adam optimizer [31] with learning rate 10^{-3} decayed by 0.99 every 2000 epochs.

188 **Datasets** We leverage two widely used benchmark datasets to evaluate the proposed model for
 189 surface reconstruction: Surface Reconstruction Benchmark (SRB) [7] and Thing10K [63]. The
 190 geometries in the mentioned datasets are challenging because of their complex topologies and
 191 incomplete observations. Following the prior works, we adopt five objects per dataset. We normalize
 192 the input data to center at zero and have a maximum norm of one.

193 **Baselines** We compare the proposed model with the following baselines: (i) IGR [23], (ii) SIREN
 194 [53], (iii) SAL [3], (iv) PHASE [35], (v) DiGS [6], and (vi) VisCo [47] from only raw point cloud
 195 data without normal vectors.

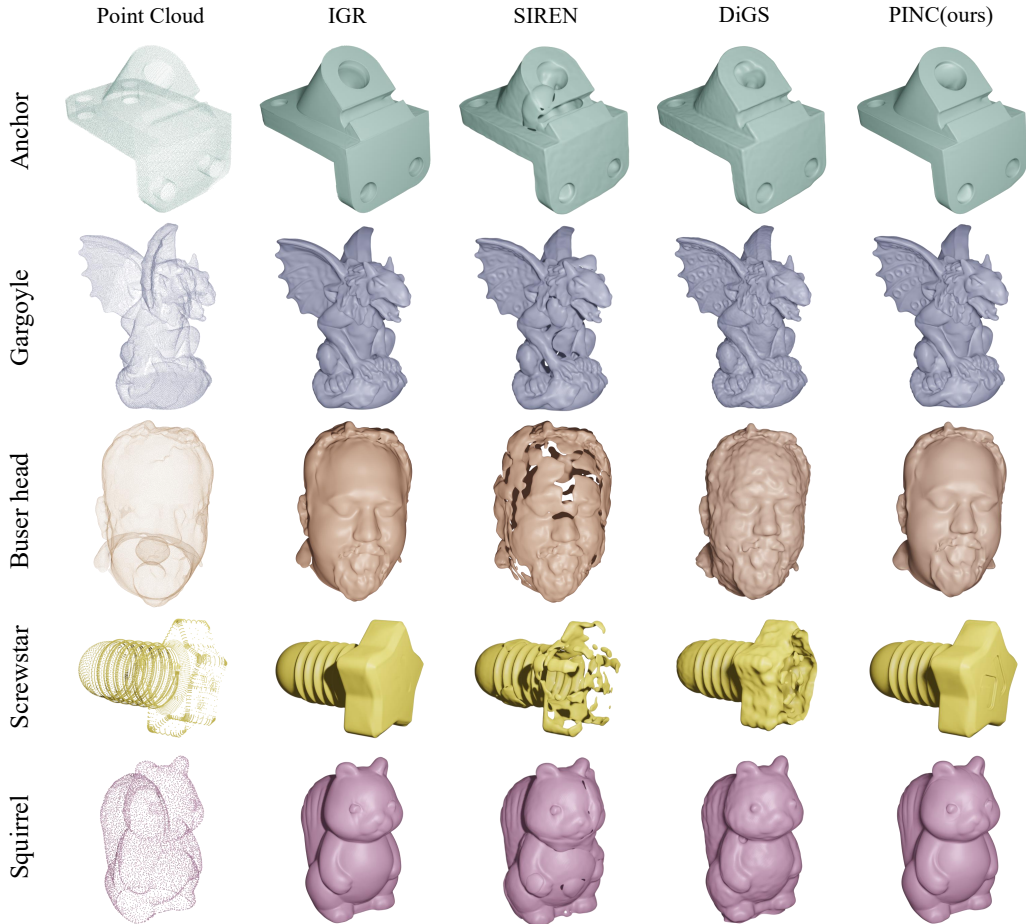


Figure 3: 3D Reconstruction results for SRB and Thingi10K datasets.

196 **Metrics** To estimate the quantitative accuracy of the reconstructed surface, we measure Chamfer
 197 (d_C) and Hausdorff (d_H) distances between the ground-truth point clouds and the reconstructed
 198 surfaces. Moreover, we report one-sided distances $d_{\vec{C}}$ and $d_{\vec{H}}$ between the noisy data and the
 199 reconstructed surfaces. Please see Appendix A.2 for precise definitions.

200 4.1 Surface reconstruction

201 We validate the performance of the proposed PINC (13) in surface reconstruction in comparison to
 202 other INR baselines. For a fair comparison, we consider the baseline models that were trained without
 203 a normal prior. Table 1 summarizes the numerical comparison on SRB in terms of metrics. We report
 204 the results of baselines from [35, 47, 6]. The results show that the reconstruction quality obtained is
 205 on par with the leading INRs, and we achieved state-of-the-art performance for Chamfer distances.

206 We further verify the accuracy of the reconstructed surface for the Thingi10K dataset by measuring
 207 the metrics. For Thingi10K, we reproduce the results of IGR, SIREN, and DiGS without normal
 208 vectors using the official codes. Results on Thingi10K presented in Table 2 show the proposed
 209 method achieves superior performance compared to existing approaches. PINC achieves similar or
 210 better metric values on all objects.

211 The qualitative results are presented in Figure 3. SIREN, which imposes high-frequency features to
 212 the model by using a sine periodic function as activation, restores a somewhat torn surface. Similarly,
 213 DiGS restores rough and ragged surfaces, for example, the human face and squirrel body are not
 214 smooth and are rendered unevenly. On the other hand, IGR provides smooth surfaces but tends to
 215 over-smooth details such as the gargoyle’s wings and detail on the star-shaped bolt head of screwstar.

Table 1: Results on surface reconstruction of SRB.

Model	Anchor				Daratech				DC				Gargoyle				Loard Quas			
	GT		Scans		GT		Scans		GT		Scans		GT		Scans		GT		Scans	
	d_C	d_H	$d_{\vec{C}}$	$d_{\vec{H}}$																
IGR	0.45	7.45	0.17	4.55	4.9	42.15	0.7	3.68	0.63	10.35	0.14	3.44	0.77	17.46	0.18	2.04	0.16	4.22	0.08	1.14
SIREN	0.72	10.98	0.11	1.27	0.21	4.37	0.09	1.78	0.34	6.27	0.06	2.71	0.46	7.76	0.08	0.68	0.35	8.96	0.06	0.65
SAL	0.42	7.21	0.17	4.67	0.62	13.21	0.11	2.15	0.18	3.06	0.08	2.82	0.45	9.74	0.21	3.84	0.13	4.14	0.07	4.04
PHASE	0.29	7.43	0.09	1.49	0.35	7.24	0.08	1.21	0.19	4.65	0.05	2.78	0.17	4.79	0.07	1.58	0.11	0.71	0.05	0.74
DiGS	0.29	7.19	0.11	1.17	0.20	3.72	0.09	1.80	0.15	1.70	0.07	2.75	0.17	4.10	0.09	0.92	0.12	0.91	0.06	0.70
VisCO	0.21	3.00	0.15	1.07	0.26	4.06	0.14	1.76	0.15	2.22	0.09	2.76	0.17	4.40	0.11	0.96	0.12	1.06	0.7	0.64
PINC	0.29	7.54	0.09	1.20	0.37	7.24	0.11	1.88	0.14	2.56	0.04	2.73	0.16	4.78	0.05	0.80	0.10	0.92	0.04	0.67

Table 2: Results on surface reconstruction of Thingi10K.

Model	Squirrel		Buser head		Screwstar		Frogrock		Pumpkin	
	d_C	d_H	d_C	d_H	d_C	d_H	d_C	d_H	d_C	d_H
IGR	0.36	11.97	0.38	5.95	0.18	3.02	0.48	12.05	0.11	1.13
SIREN	0.47	5.66	0.43	4.81	0.27	4.98	0.78	14.75	0.46	5.03
DiGS	0.50	12.45	0.39	10.64	0.26	6.33	0.45	10.50	0.32	8.03
PINC	0.35	11.55	0.37	6.19	0.17	3.00	0.43	11.06	0.10	1.90

216 The results confirm that the proposed PINC (13) adopts both of these advantages: PINC represents a
 217 smooth and detailed surface. More results can be found in the appendix.

218 4.2 Reconstruction from noisy data

219 In this section, we analyze whether the proposed PINC (13) produces robust results to the presence of
 220 noise in the input point data. In many situations, the samples obtained by the scanning process contain
 221 a lot of noise and inaccurate surface normals are estimated from these noisy samples. Therefore, it is
 222 an important task to perform accurate reconstruction using only noisy data without normal vectors.
 223 To investigate the robustness to noise, we perturb the data with additive Gaussian noise with mean
 224 zero and two standard deviations 0.005 and 0.01.

225 We quantify the ability of the proposed model to handle noise in the input points. The qualitative
 226 results are shown in Figure 4. Compared to existing methods, the results demonstrate superior
 227 resilience of the proposed model with respect to noise corruption in the input samples. We can
 228 observe that SIREN and DiGS restore broken surfaces that appear to be small grains as the noise
 229 level increases. On the other hand, the proposed model produces a relatively smooth reconstruction.
 230 Results show that PINC is less sensitive to noise than others.

231 4.3 Ablation studies

232 This section is devoted to ablation analyses which show that each part of the proposed loss function
 233 $\mathcal{L}_{\text{total}}$ in conjunction with the divergence-free splitting architecture plays an important role in high-
 234 quality reconstruction.

235 **Effect of curl-free constraint** We first study the effect of the curl-free constraint on reconstructing
 236 high fidelity surfaces. To investigate the effectiveness of the proposed curl-free constraint, we
 237 compare the performance of PINC without the curl-free loss term, i.e., the model trained with the loss
 238 function $\mathcal{L}_{p\text{-Poisson}}$ (8). The results on the SRB dataset are depicted in Figure 5. The variable splitting
 239 method, which satisfies the p -Poisson equation as a hard constraint (without the curl-free condition),
 240 recovers a fairly decent surface, but it generates oversmoothed surfaces and details are lost. However,
 241 as we can see from the result reconstructed with the curl-free constraint, this constraint allows us to
 242 capture the details that PINC without the curl-free condition cannot recover.

243 **Effect of minimal area criterion** We study the effect of the minimal area criterion suggested in
 244 Section 3.3. In real scenarios, there are defected regions where the surface has not been measured. To
 245 fill this part of the hole, the minimum surface area is considered. Figure 6 clearly shows this effect.
 246 Some parts in the daratech of SRB have a hole in the back. Probably because of this hole, parts that
 247 are not manifolds are spread out as manifolds as shown in the left figure without considering the

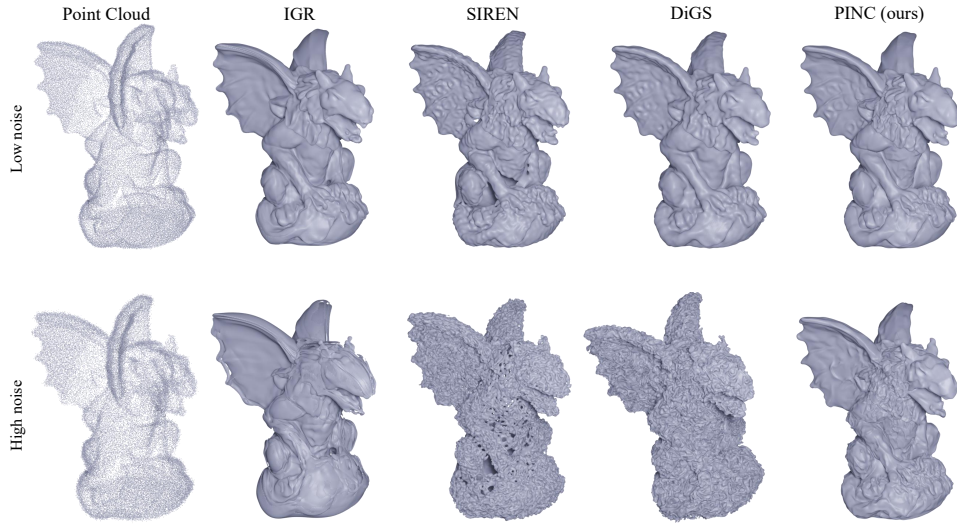


Figure 4: Reconstruction results from noisy observations. Two levels of additive Gaussian noise with standard deviations $\sigma = 0.005$ (low) and 0.01 (high) are considered.

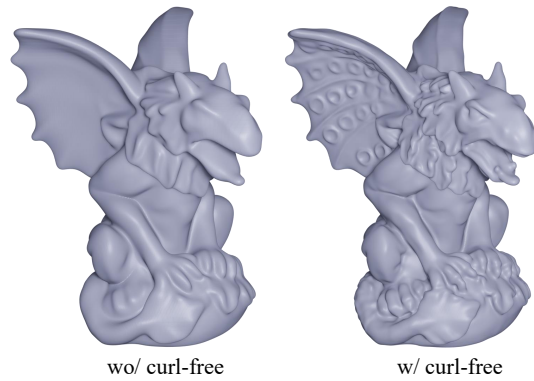


Figure 5: Comparison of surface reconstruction without (left) and with (right) curl-free constraint.

248 minimal area. However, we can see that adding a minimal area loss term alleviates this problem. We
 249 would like to note that, except for daratech, we did not encounter this problem because other data
 250 are point clouds sampled from a closed surface and also are not related to hole filling. Indeed, we
 251 empirically observe that the results are quite similar with and without the minimal area term for all
 252 data other than daratech.

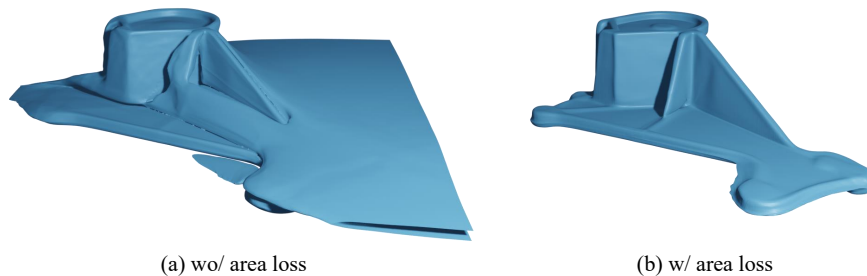


Figure 6: Comparison of surface recovery without (a) and with (b) minimum area criterion.

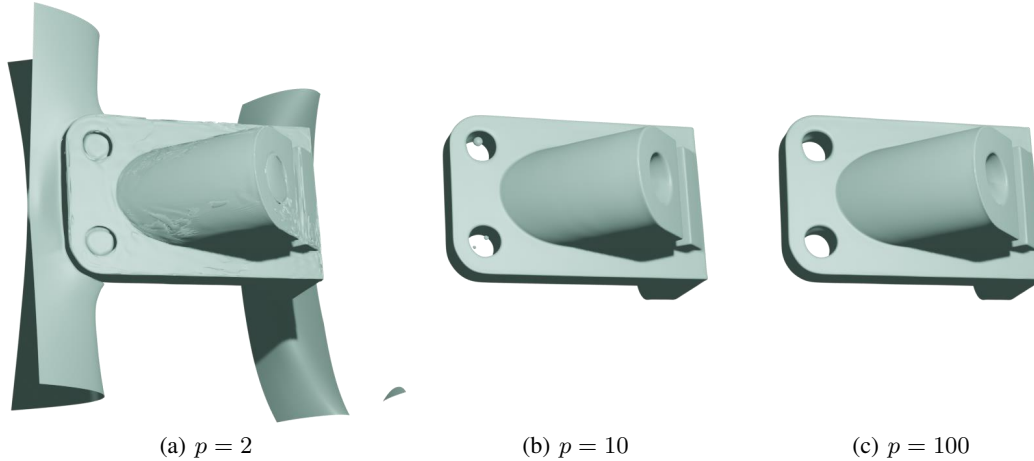


Figure 7: Surface reconstruction of anchor data with various p . The results show the importance of using a sufficiently large p for an accurate approximation.

253 **Effect of large p** The p -Poisson equation (1) draws the SDF as p becomes infinitely large. Therefore,
 254 it is natural to think that it would be good to use a large p . Here, we conducted experiments on the
 255 effect of p . We define G with various $p = 2, 10,$ and 100 and learn the SDF with it. Figure 7 shows
 256 surfaces that were recovered from the Gargoyle data in the SRB with different p values. When p is
 257 as small as 2, it is obvious that it is difficult to reconstruct a compact surface from points. When p
 258 is 10, a much better surface is constructed than that of $p = 2$, but the by-products still remain on
 259 the small holes. Furthermore, a large value of $p = 100$ provides a quite proper reconstruction. This
 260 experimental result demonstrates that a more accurate approximation can be obtained by the use of a
 261 large p , which is consistent with the theory. This once again highlights the advantage of the variable
 262 splitting method we have proposed, which allows an arbitrarily large p to be used. This highlights
 263 the advantage of the variable splitting method (7) we have proposed in Section 3.1, which allows an
 264 arbitrarily large p to be used. Note that the previous approaches have not been able to use large p
 265 because the numeric value of p -power easily exceeds the limit of floating precision. On the other
 266 hand, the proposed method is amenable to large p and hence the reconstruction becomes closer to the
 267 point cloud.

268 5 Conclusion and limitations

269 We presented a p -Poisson equation-based shape representation learning, termed PINC, that recon-
 270 structs high-fidelity surfaces using only the locations of given points. We introduced the gradient of
 271 the SDF as an auxiliary network output and incorporated the p -Poisson equation into the auxiliary
 272 variable as a hard constraint. The curl-free constraint was also used to provide a more accurate
 273 representation. Furthermore, the minimal surface area regularization was considered to provide a
 274 compact surface and overcome the ill-posedness of the surface reconstruction problem caused by
 275 unobserved points. The proposed PINC successively achieved a faithful surface with intricate details
 276 and was robust to noisy observations.

277 The minimization of the surface area is used to reconstruct missing parts of points under the as-
 278 sumption that a point cloud is measured by a closed surface. Regarding the hole-filling strategy,
 279 it still needs further discussion and investigation of various constraints such as mean curvature or
 280 total variation of the gradient. At present, the proposed PDE-based framework is limited to closed
 281 surfaces and is inadequate to reconstruct open surfaces. We leave the development to open surface
 282 reconstruction as future work. Establishing a neural network initialization that favors the auxiliary
 283 gradient of the SDF would be an interesting venue.

284 **References**

- 285 [1] Nina Amenta and Marshall Bern. Surface reconstruction by Voronoi filtering. In *Proceedings*
286 *of the Fourteenth Annual Symposium on Computational Geometry*, pages 39–48, 1998.
- 287 [2] Matan Atzmon, Niv Haim, Lior Yariv, Ofer Israelov, Haggai Maron, and Yaron Lipman.
288 Controlling neural level sets. *Advances in Neural Information Processing Systems*, 32, 2019.
- 289 [3] Matan Atzmon and Yaron Lipman. SAL: Sign agnostic learning of shapes from raw data. In
290 *Proceedings of the IEEE/CVF Conference on Computer Vision and Pattern Recognition*, pages
291 2565–2574, 2020.
- 292 [4] Matan Atzmon and Yaron Lipman. SALD: Sign agnostic learning with derivatives. *arXiv*
293 *preprint arXiv:2006.05400*, 2020.
- 294 [5] Alexander G. Belyaev and Pierre-Alain Fayolle. On variational and PDE-based distance
295 function approximations. In *Computer Graphics Forum*, volume 34, pages 104–118. Wiley
296 Online Library, 2015.
- 297 [6] Yizhak Ben-Shabat, Chamin Hewa Koneputugodage, and Stephen Gould. DiGS: Divergence
298 guided shape implicit neural representation for unoriented point clouds. In *2022 IEEE/CVF*
299 *Conference on Computer Vision and Pattern Recognition (CVPR)*, pages 19301–19310, 2022.
- 300 [7] Matthew Berger, Joshua A Levine, Luis Gustavo Nonato, Gabriel Taubin, and Claudio T Silva.
301 A benchmark for surface reconstruction. *ACM Transactions on Graphics (TOG)*, 32(2):1–17,
302 2013.
- 303 [8] Matthew Berger, Andrea Tagliasacchi, Lee M. Seversky, Pierre Alliez, Gael Guennebaud,
304 Joshua A Levine, Andrei Sharf, and Claudio T Silva. A survey of surface reconstruction from
305 point clouds. In *Computer graphics forum*, volume 36, pages 301–329. Wiley Online Library,
306 2017.
- 307 [9] Matthew Berger, Andrea Tagliasacchi, Lee M. Seversky, Pierre Alliez, Joshua A. Levine, Andrei
308 Sharf, and Claudio T. Silva. State of the art in surface reconstruction from point clouds. In *35th*
309 *Annual Conference of the European Association for Computer Graphics, Eurographics 2014 -*
310 *State of the Art Reports*. The Eurographics Association, 2014.
- 311 [10] Fausto Bernardini, Joshua Mittleman, Holly Rushmeier, Cláudio Silva, and Gabriel Taubin.
312 The ball-pivoting algorithm for surface reconstruction. *IEEE transactions on visualization and*
313 *computer graphics*, 5(4):349–359, 1999.
- 314 [11] Tilak Bhattacharya, Emmanuele DiBenedetto, and Juan Manfredi. Limits as $p \rightarrow \infty$ of
315 $\Delta_p u_p = f$ and related external problems. *Rendiconti del Seminario Matematico Università e*
316 *Politecnico di Torino*, 47:15–68, 1989.
- 317 [12] Stephen Boyd, Neal Parikh, Eric Chu, Borja Peleato, Jonathan Eckstein, et al. Distributed opti-
318 mization and statistical learning via the alternating direction method of multipliers. *Foundations*
319 *and Trends® in Machine learning*, 3(1):1–122, 2011.
- 320 [13] Stephen Boyd and Lieven Vandenberghhe. *Convex optimization*. Cambridge University Press,
321 2004.
- 322 [14] Fatih Calakli and Gabriel Taubin. SSD: Smooth signed distance surface reconstruction. In
323 *Computer Graphics Forum*, volume 30, pages 1993–2002. Wiley Online Library, 2011.
- 324 [15] Vicent Caselles, Gloria Haro, Guillermo Sapiro, and Joan Verdera. On geometric variational
325 models for inpainting surface holes. *Computer Vision and Image Understanding*, 111(3):351–
326 373, 2008.
- 327 [16] Zhiqin Chen and Hao Zhang. Learning implicit fields for generative shape modeling. In
328 *Proceedings of the IEEE/CVF Conference on Computer Vision and Pattern Recognition*, pages
329 5939–5948, 2019.

- 330 [17] Alexander G. Churbanov and Petr N. Vabishchevich. Numerical solution of boundary value
331 problems for the eikonal equation in an anisotropic medium. *Journal of Computational and*
332 *Applied Mathematics*, 362:55–67, 2019.
- 333 [18] Tamal K. Dey, Gang Li, and Jian Sun. Normal estimation for point clouds: A comparison study
334 for a voronoi based method. In *Proceedings Eurographics/IEEE VGTC Symposium Point-Based*
335 *Graphics*, pages 39–46. IEEE, 2005.
- 336 [19] Philipp Erler, Paul Guerrero, Stefan Ohrhallinger, Niloy J Mitra, and Michael Wimmer.
337 Points2surf learning implicit surfaces from point clouds. In *Computer Vision–ECCV 2020: 16th*
338 *European Conference, Glasgow, UK, August 23–28, 2020, Proceedings, Part V*, pages 108–124.
339 Springer, 2020.
- 340 [20] Pierre-Alain Fayolle. Signed distance function computation from an implicit surface. *arXiv*
341 *preprint arXiv:2104.08057*, 2021.
- 342 [21] Henry Fuchs, Zvi M Kedem, and Samuel P Uselton. Optimal surface reconstruction from planar
343 contours. *Communications of the ACM*, 20(10):693–702, 1977.
- 344 [22] Tom Goldstein and Stanley Osher. The split Bregman method for L1-regularized problems.
345 *SIAM journal on imaging sciences*, 2(2):323–343, 2009.
- 346 [23] Amos Gropp, Lior Yariv, Niv Haim, Matan Atzmon, and Yaron Lipman. Implicit geometric
347 regularization for learning shapes. ICML’20, page 11. JMLR.org, 2020.
- 348 [24] Jooyoung Hahn, Karol Mikula, and Peter Frolkovič. Laplacian regularized eikonal equation
349 with Soner boundary condition on polyhedral meshes. *arXiv preprint arXiv:2301.11656*, 2023.
- 350 [25] Jooyoung Hahn, Jie Qiu, Eiji Sugisaki, Lei Jia, Xue-Cheng Tai, and Hock Soon Seah. Stroke-
351 based surface reconstruction. *Numerical Mathematics: Theory, Methods and Applications*,
352 6:297–324, 2013.
- 353 [26] Yuchen He, Sung Ha Kang, and Hao Liu. Curvature regularized surface reconstruction from
354 point clouds. *SIAM Journal on Imaging Sciences*, 13(4):1834–1859, 2020.
- 355 [27] Hugues Hoppe, Tony DeRose, Tom Duchamp, John McDonald, and Werner Stuetzle. Surface
356 reconstruction from unorganized points. In *Proceedings of the 19th annual conference on*
357 *computer graphics and interactive techniques*, pages 71–78, 1992.
- 358 [28] Hui Huang, Dan Li, Hao Zhang, Uri Ascher, and Daniel Cohen-Or. Consolidation of unorganized
359 point clouds for surface reconstruction. *ACM transactions on graphics (TOG)*, 28(5):1–7, 2009.
- 360 [29] Bernhard Kawohl. On a family of torsional creep problems. *Journal für die reine und ange-*
361 *wandte Mathematik*, 410:1–22, 1990.
- 362 [30] Michael Kazhdan, Matthew Bolitho, and Hugues Hoppe. Poisson surface reconstruction. In
363 *Proceedings of the fourth Eurographics symposium on Geometry processing*, volume 7, 2006.
- 364 [31] Diederik P. Kingma and Jimmy Ba. Adam: A method for stochastic optimization. *arXiv preprint*
365 *arXiv:1412.6980*, 2014.
- 366 [32] Leo Koenigsberger. *Hermann von Helmholtz*. Clarendon pPress, 1906.
- 367 [33] Aditi Krishnapriyan, Amir Gholami, Shandian Zhe, Robert Kirby, and Michael W Mahoney.
368 Characterizing possible failure modes in physics-informed neural networks. *Advances in Neural*
369 *Information Processing Systems*, 34:26548–26560, 2021.
- 370 [34] Marc Levoy, Kari Pulli, Brian Curless, Szymon Rusinkiewicz, David Koller, Lucas Pereira,
371 Matt Ginzton, Sean Anderson, James Davis, Jeremy Ginsberg, Jonathan Shade, and Duane Fulk.
372 The digital Michelangelo project: 3D scanning of large statues. In *Proceedings of the 27th*
373 *Annual Conference on Computer Graphics and Interactive Techniques, SIGGRAPH ’00*, pages
374 131–144, USA, 2000. ACM Press/Addison-Wesley Publishing Co.
- 375 [35] Yaron Lipman. Phase transitions, distance functions, and implicit neural representations. In
376 *International Conference on Machine Learning*, 2021.

- 377 [36] William E. Lorensen and Harvey E. Cline. Marching cubes: A high resolution 3D surface
378 construction algorithm. *ACM SIGGRAPH computer graphics*, 21(4):163–169, 1987.
- 379 [37] Baorui Ma, Zhizhong Han, Yu-Shen Liu, and Matthias Zwicker. Neural-Pull: Learning signed
380 distance functions from point clouds by learning to pull space onto surfaces. In *International
381 Conference on Machine Learning*, 2020.
- 382 [38] Zoltan Csaba Marton, Radu Bogdan Rusu, and Michael Beetz. On fast surface reconstruction
383 methods for large and noisy point clouds. In *2009 IEEE international conference on robotics
384 and automation*, pages 3218–3223. IEEE, 2009.
- 385 [39] Lars Mescheder, Michael Oechsle, Michael Niemeyer, Sebastian Nowozin, and Andreas Geiger.
386 Occupancy networks: Learning 3D reconstruction in function space. In *Proceedings of the
387 IEEE/CVF conference on computer vision and pattern recognition*, pages 4460–4470, 2019.
- 388 [40] Mateusz Michalkiewicz, Jhony K Pontes, Dominic Jack, Mahsa Baktashmotlagh, and Anders
389 Eriksson. Deep Level Sets: Implicit surface representations for 3D shape inference. *CoRR*,
390 2019.
- 391 [41] Carsten Moenning and Neil A. Dodgson. Fast marching farthest point sampling for implicit
392 surfaces and point clouds. *Computer Laboratory Technical Report*, 565:1–12, 2003.
- 393 [42] Jeong Joon Park, Peter Florence, Julian Straub, Richard Newcombe, and Steven Lovegrove.
394 DeepSDF: Learning continuous signed distance functions for shape representation. In *Proceed-
395 ings of the IEEE/CVF conference on computer vision and pattern recognition*, pages 165–174,
396 2019.
- 397 [43] Yesom Park, Chang Hoon Song, Jooyoung Hahn, and Myungjoo Kang. ReSDF: Redistancing
398 implicit surfaces using neural networks. *arXiv preprint arXiv:2305.08174*, 2023.
- 399 [44] Adam Paszke, Sam Gross, Soumith Chintala, Gregory Chanan, Edward Yang, Zachary DeVito,
400 Zeming Lin, Alban Desmaison, Luca Antiga, and Adam Lerer. Automatic differentiation in
401 pytorch. 2017.
- 402 [45] Donald W. Peaceman and Henry H. Rachford, Jr. The numerical solution of parabolic and
403 elliptic differential equations. *Journal of the Society for Industrial and Applied Mathematics*,
404 3(1):28–41, 1955.
- 405 [46] Songyou Peng, Chiyu Jiang, Yiyi Liao, Michael Niemeyer, Marc Pollefeys, and Andreas Geiger.
406 Shape As Points: A differentiable Poisson solver. *Advances in Neural Information Processing
407 Systems*, 34:13032–13044, 2021.
- 408 [47] Albert Pumarola, Artsiom Sanakoyeu, Lior Yariv, Ali K. Thabet, and Yaron Lipman. VisCo
409 grids: Surface reconstruction with viscosity and coarea grids. In *NeurIPS*, 2022.
- 410 [48] Fu Qiancheng, Xu Qingshan, Ong Yew-Soon, and Tao Wenbing. Geo-Neus: Geometry-
411 consistent neural implicit surfaces learning for multi-view reconstruction. *Advances in Neural
412 Information Processing Systems*, 35:3403–3416, 2022.
- 413 [49] Maziar Raissi, Paris Perdikaris, and George E Karniadakis. Physics-informed neural networks:
414 A deep learning framework for solving forward and inverse problems involving nonlinear partial
415 differential equations. *Journal of Computational physics*, 378:686–707, 2019.
- 416 [50] Jack Richter-Powell, Yaron Lipman, and Ricky T. Q. Chen. Neural conservation laws: A
417 divergence-free perspective. In *Advances in Neural Information Processing Systems*, 2022.
- 418 [51] Liu Shaohui, Zhang Yinda, u Peng Songyo, Shi Boxin, Pollefeys Marc, and Cui. Zhaopeng.
419 DIST: Rendering deep implicit signed distance function with differentiable sphere tracing.
420 *IEEE/CVF Conference on Computer Vision and Pattern Recognition*, pages 2019–2028, 2020.
- 421 [52] Vincent Sitzmann, Eric R. Chan, Richard Tucker, Noah Snively, and Gordon Wetzstein.
422 MetaSDF: Meta-learning signed distance functions. *Advances in Neural Information Pro-
423 cessing Systems*, 2020.

- 424 [53] Vincent Sitzmann, Julien N. P. Martel, Alexander W. Bergman, David B. Lindell, and Gordon
425 Wetzstein. Implicit neural representations with periodic activation functions. In *Proceedings of*
426 *the 34th International Conference on Neural Information Processing Systems*, number 626 in
427 NIPS'20, Red Hook, NY, USA, 2020. Curran Associates Inc.
- 428 [54] Matthew Tancik, Pratul Srinivasan, Ben Mildenhall, Sara Fridovich-Keil, Nithin Raghavan,
429 Utkarsh Singhal, Ravi Ramamoorthi, Jonathan Barron, and Ren Ng. Fourier features let
430 networks learn high frequency functions in low dimensional domains. *Advances in Neural*
431 *Information Processing Systems*, 33:7537–7547, 2020.
- 432 [55] J. Van Bladel. On Helmholtz's theorem in finite regions. Technical report, CM-P00066539,
433 1958.
- 434 [56] He Wang, Srinath Sridhar, Jingwei Huang, Julien Valentin, Shuran Song, and Leonidas J Guibas.
435 Normalized object coordinate space for category-level 6D object pose and size estimation. In
436 *Proceedings of the IEEE/CVF Conference on Computer Vision and Pattern Recognition*, pages
437 2642–2651, 2019.
- 438 [57] Sifan Wang, Yujun Teng, and Paris Perdikaris. Understanding and mitigating gradient flow
439 pathologies in physics-informed neural networks. *SIAM Journal on Scientific Computing*,
440 43(5):A3055–A3081, 2021.
- 441 [58] Yilun Wang, Junfeng Yang, Wotao Yin, and Yin Zhang. A new alternating minimization
442 algorithm for total variation image reconstruction. *SIAM Journal on Imaging Sciences*, 1(3):248–
443 272, 2008.
- 444 [59] Qiangeng Xu, Weiyue Wang, Duygu Ceylan, Radomir Mech, and Ulrich Neumann. DISN:
445 Deep implicit surface network for high-quality single-view 3D reconstruction. *Advances in*
446 *neural information processing systems*, 32, 2019.
- 447 [60] Lior Yariv, Yoni Kasten, Dror Moran, Meirav Galun, Matan Atzmon, Basri Ronen, and Yaron
448 Lipman. Multiview neural surface reconstruction by disentangling geometry and appearance.
449 *Advances in Neural Information Processing Systems*, 33:2492–2502, 2020.
- 450 [61] Jingyang Zhang, Yao Yao, Shiwei Li, Tian Fang, David McKinnon, Yanghai Tsin, and Long
451 Quan. Critical regularizations for neural surface reconstruction in the wild. In *Proceedings*
452 *of the IEEE/CVF Conference on Computer Vision and Pattern Recognition*, pages 6270–6279,
453 2022.
- 454 [62] Hong-Kai Zhao, Stanley Osher, and Ronald Fedkiw. Fast surface reconstruction using the level
455 set method. In *Proceedings IEEE Workshop on Variational and Level Set Methods in Computer*
456 *Vision*, pages 194–201. IEEE, 2001.
- 457 [63] Qingnan Zhou and Alec Jacobson. Thingi10k: A dataset of 10,000 3D-printing models. *arXiv*
458 *preprint arXiv:1605.04797*, 2016.

459 A Implementation Details

460 In this section, we provide more details about the implementation for reproducibility. Note that our
461 code is built on top of IGR¹ (MIT License).

462 A.1 Experimental Setup

463 **Parameter Tuning** The proposed training loss $\mathcal{L}_{\text{total}}$ (13) is a weighted sum of five loss terms
464 with four regularization parameters $\lambda_1, \lambda_2, \lambda_3$, and λ_4 . In all surface reconstruction experiments,
465 we use $\lambda_1 = 0.1$, $\lambda_2 = 0.0001$, $\lambda_3 = 0.0005$, and $\lambda_4 = 0.1$. In the proposed model, p is also a
466 hyperparameter to be chosen. Considering the theoretical fact that p should be infinitely large and
467 numerical simplicity, we set $p = \infty$. We empirically confirm no significant difference between when
468 $p = 100$ and when $p = \infty$. Moreover, we set the smoothing parameter $\epsilon = 1$ for approximating
469 Dirac delta in (13).

470 **Network Architecture** As in previous studies [42, 23, 35], we represent the primary and auxiliary
471 outputs by a single 8-layered multi-layer perceptron (MLP) $\mathbb{R}^3 \rightarrow \mathbb{R}^7$ with 512 neurons and a skip
472 connection to the fourth layer, but only the output dimension of the last layer is increased by six due to
473 the two auxiliary variables; see Figure 2. We use softplus activation function $\alpha(x) = \frac{1}{\beta} \ln(1 + e^{\beta x})$
474 with $\beta = 100$. Network weights are initialized by the geometric initialization proposed in [3].

475 **Training details** The gradient and the curl of networks are computed with auto-differentiation
476 library (autograd) [44]. In all experiments, we use the Adam optimizer [31] with learning rate 10^{-3}
477 decayed by 0.99 every 2,000 epochs. At each iteration, we uniform randomly sample 16,384 points
478 $\mathbf{x} \in \mathcal{X}$ from the point cloud \mathcal{X} . We sample the collocation points of Ω as provided in [23]. The
479 collocation points consist of global points and local points. The local collocation points are sampled
480 by perturbing each of the 16,384 points drawn from the point cloud with a zero mean Gaussian
481 distribution with a standard deviation equal to the distance to the 50th nearest neighbor. The global
482 collocation points are made up of approximately 2,000 points from the uniform distribution $U(-\eta, \eta)$
483 with $\eta = 1.1$.

484 **Baseline models** For baseline models on the Thing10K dataset, we use the official codes of IGR¹
485 (MIT License), SIREN² (MIT License), and DiGS³ (MIT License). We faithfully follow the official
486 implementation to train each model without normal prior. For the variable splitting representation of
487 the eikonal equation (9), there is a single auxiliary output. Consequently, we use the same 8 layer
488 MLP with 512 nodes, but a network with an output dimension of 4. We normalize the auxiliary output
489 to make it a unit norm, and use the normalized one to represent H .

490 A.2 Evaluation

491 **Metrics** We measure the distance between two point clouds \mathcal{X} and \mathcal{Y} by using the standard one-
492 sided and double-sided ℓ_1 Chamfer distances $d_{\vec{C}}, d_C$ and Hausdorff distances $d_{\vec{H}}, d_H$. Each are
493 defined as follows:

$$\begin{aligned} d_{\vec{C}}(\mathcal{X}, \mathcal{Y}) &= \frac{1}{|\mathcal{X}|} \sum_{\mathbf{x} \in \mathcal{X}} \min_{\mathbf{y} \in \mathcal{Y}} \|\mathbf{x} - \mathbf{y}\|_2, \\ d_C(\mathcal{X}, \mathcal{Y}) &= \frac{1}{2} (d_{\vec{C}}(\mathcal{X}, \mathcal{Y}) + d_{\vec{C}}(\mathcal{Y}, \mathcal{X})), \\ d_{\vec{H}}(\mathcal{X}, \mathcal{Y}) &= \max_{\mathbf{x} \in \mathcal{X}} \min_{\mathbf{y} \in \mathcal{Y}} \|\mathbf{x} - \mathbf{y}\|_2, \\ d_H(\mathcal{X}, \mathcal{Y}) &= \max \{d_{\vec{H}}(\mathcal{X}, \mathcal{Y}) + d_{\vec{H}}(\mathcal{Y}, \mathcal{X})\}. \end{aligned}$$

494 When we estimate the distance from a surface, we sample $10M$ uniformly random points from the
495 surface and then measure the distance from the sampled point clouds by the metrics defined above.

¹<https://github.com/amosgrop/IGR>

²<https://github.com/vsitzmann/siren>

³<https://github.com/Chumbyte/DiGS>

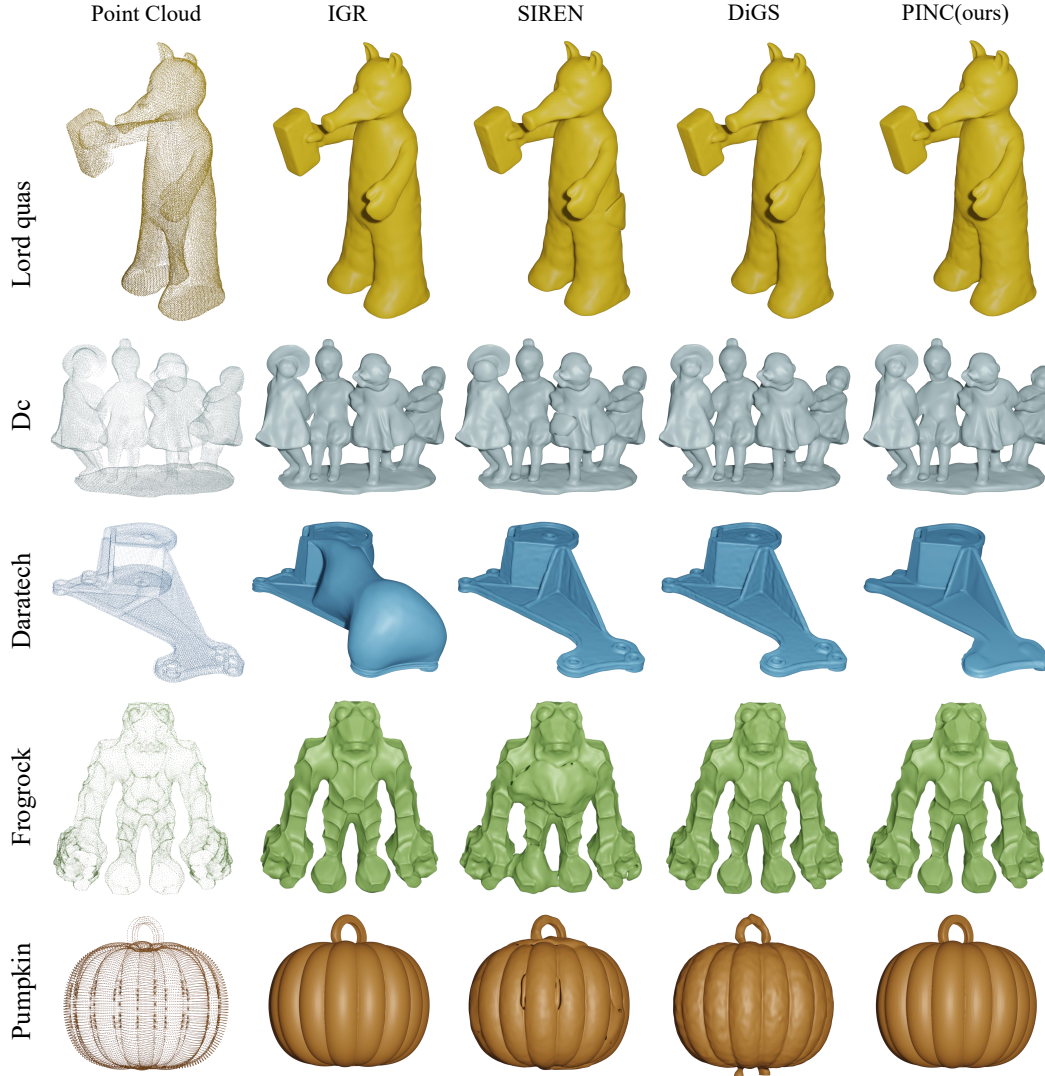


Figure 8: Additional qualitative results of the surface reconstruction on SRB and Thing10K datasets.

496 **Level set extraction** We extract the zero level set of a trained neural network u by using the
 497 classical marching cubes meshing algorithm [36] on a $512 \times 512 \times 512$ uniform grid.

498 B Additional Results

499 **Additional qualitative results** Figure 8 provides additional qualitative results of surface recon-
 500 struction on SRB and Thing10K discussed in Section 4.1.

501 **Reconstruction of large point clouds** We further provide qualitative results for surface recon-
 502 struction from large models taken from Thing10K. The adopted point clouds consist of from 35K to 980K
 503 vertices. Figure 9 depicts the qualitative reconstruction results of PINC on these large point clouds.
 504 The model is trained with the same configuration used in Section 4.1.

505 **More results on effect of p** Theoretically, an accurate SDF can be obtained as p grows infinitely.
 506 That the same story continues in practice is confirmed by the results shown in Figure 10. We can
 507 see that the larger p induces a better reconstruction. This phenomenon is also observed in Figure 7.
 508 Moreover, it can be seen that $p = \infty$, which we used in the implementation, gives a similar qualitative



Figure 9: Reconstructed surfaces of large models from Thingi10K.

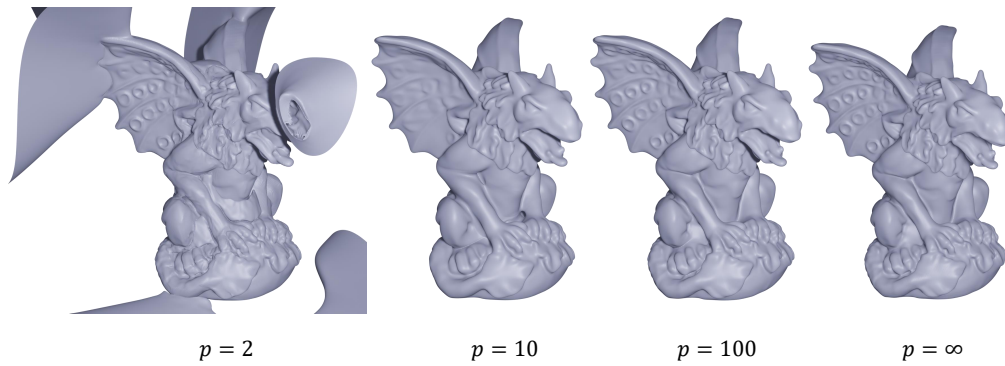


Figure 10: Quality of surface reconstruction with varying p from $p = 2$ to $p = \infty$.

509 result to $p = 100$. These experimental results once again remind us how important it is to be able to
 510 use a large p .

511 Furthermore, we provide numerical verification for the use of $p = \infty$ in Figure 11. For notational
 512 convenience, we use the subscript u_p to denote the dependence of the solution on the parameter p .
 513 Figure 11 depicts graphs of the mean squared error (MSE) of u_p and u_∞ over different p . MSEs are
 514 computed by discretizing the computational domain Ω into a $100 \times 100 \times 100$ uniform grid. The
 515 results show that the MSE decreases as p increases. In other words, it confirms that u_p is getting
 516 closer to u_∞ as p grows, which supports the justification for using $p = \infty$.

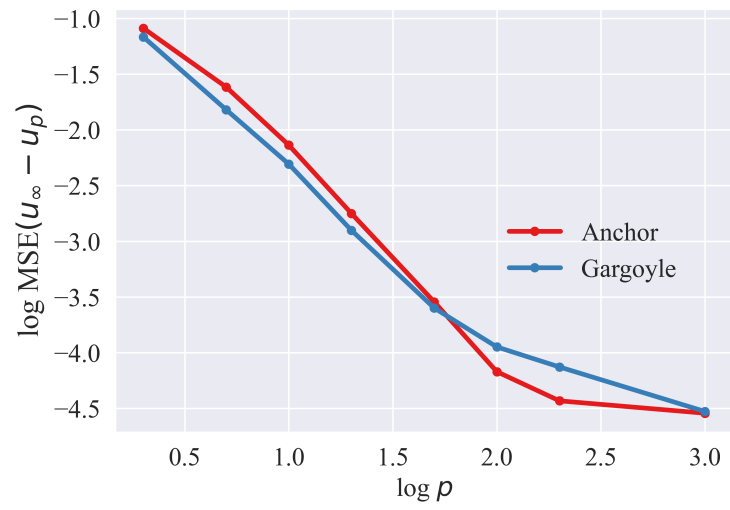


Figure 11: MSEs of u_p and u_∞ over different p .